Chapter 8

Wake Topology and Aerodynamic Performance of Finite-Span Flapping Wings

In this chapter, we extend the two-dimensional results presented in the previous chapter to three-dimensional rigid finite-span flapping wings. We investigate the wake topology behind low aspect ratio flapping wings and their dependence on the Strouhal number and flapping parameters. We also present some results on the aerodynamic performance of flapping wings and establish the best criteria for vortical structures identification.

8.1 Overview

The three-dimensional flow features generated by finite-span wings present a great challenge due to the computational effort required to compute the complex flows generated as a function of the flapping kinematics, flapping frequency, flapping amplitude, wing geometry and Reynolds number; all these factors influence the wake topology and aerodynamic performance of finite-span flapping wings. Hereafter, we study the validity of the Strouhal number St as the fundamental aerodynamic parameter for finite-span flapping wings at low Reynolds number. We also conduct several numerical experiments in order to investigate the wake topology and aerodynamic performance of rigid finite-span wings undergoing pure heaving motion, coupled heaving-and-pitching motion and rolling motion (root-flapping).

8.2 Computational Domain and Grid Setup

The overlapping grid system used for the three-dimensional flapping wings studies, is based in the two-dimensional overlapping grid system used previously, and provides good resolution in the area around the moving wing as well as in the wake region. In figures 8.1 and 8.2 we show the overlapping grid system layout, where the background grid extends $2.5 \times c$ away from the wing leading edge, $6.5 \times c$ away from the wing trailing edge, $1.5 \times c$ away from the wing-tips and $3.0 \times c$ away from the wing upper and lower surface (where c is the mean wing chord). The previous dimensions, are the dimensions for the overlapping grid system layout when the wing is in the

mean position of the flapping motion and where h_a is assumed to be equal to 0.25.

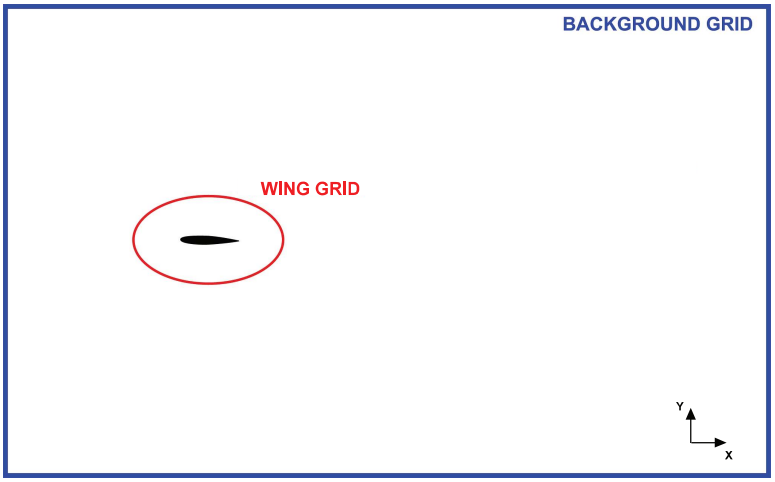

Figure 8.1: *Three-dimensional computational domain layout in the xy plane.*

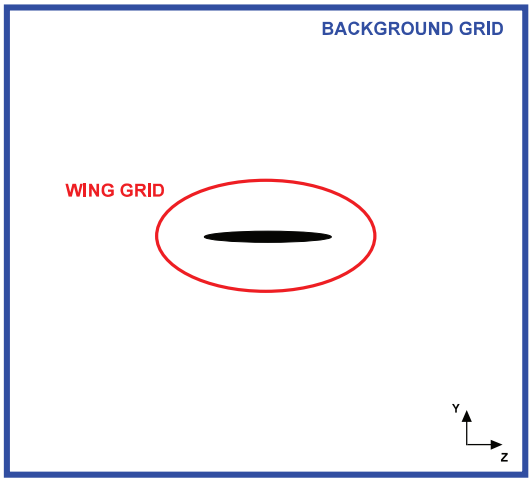

Figure 8.2: *Three-dimensional computational domain layout in the zy plane.*

The nominal grid size employed for the background grid is $160 \times 100 \times 60$ (in the x, y and z directions respectively). For the wing grid, the grid size is about $160 \times 80 \times 60$; this grid size is based on a rectangular wing of aspect ratio equal AR $= 1$ and wing chord equal to $c = 1$. In the case of a bigger or smaller domain, the grid dimensions are scaled in order to keep the same grid spacing as for this domain. The first node normal to the wing surface is placed at a distance equal to $0.0001 \times c$ (which still is in the asymptotic range of convergence as seen in Chapter 6, Section 3), and we clustered up to 14 points in the direction normal to the airfoil surface. In order to better resolve the wing wake, we use grid stretching in the x, y and z directions of the background grid (see figure 8.3). All the flapping wings calculations were started from a fully converged stationary

wing solution. In figure 8.1 the top, bottom and right boundaries are outflow boundaries and the left boundary is inflow with $(u, v, w) = (1.0, 0.0, 0.0)$, whereas in figure 8.2 all the boundaries correspond to outflow. On the wing surface we impose a no-slip boundary condition.

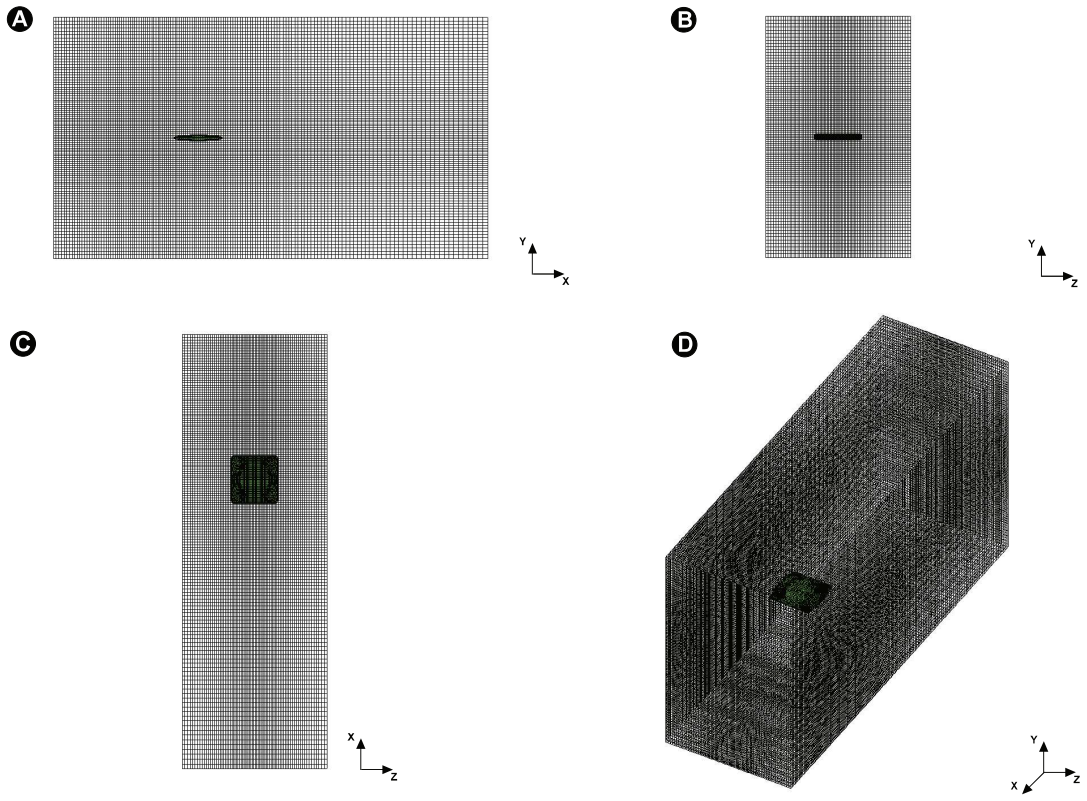

Figure 8.3: *Typical grid system employed in the current three-dimensional study. A) Side view. B) Front view. C) Top view. D) Perspective view.*

8.3 Vortex Identification

A key aspect in the study of the wake topology of finite-span wings is the proper identification of vortical structures. Hereafter, we test four well known criteria which are based on the velocity gradient tensor $\nabla \mathbf{u}$ [40, 63, 91, 178].

1. $\mid \omega \mid$-criterion, where $\mid \omega \mid$ is the norm of the vorticity vector $\mid \omega \mid = \nabla \times \mathbf{u}$. This criterion identifies a flow region as a vortex when $\mid \omega \mid$ reaches a specified threshold.

2. Q-criterion, where Q is the second invariant of $\nabla \mathbf{u}$. It defines a region as a vortex if every point in this region has $Q > 0$. The second invariant Q is defined as

$$\mathrm{Q} = 0.5\left(\| \Omega \|^2 - \| \mathrm{S} \|^2\right) \tag{8.1}$$

where $\Omega = 0.5(\nabla\mathbf{u} - \nabla\mathbf{u}^{\mathrm{T}})$ is the rate-of-strain tensor and $\mathrm{S} = 0.5(\nabla\mathbf{u} + \nabla\mathbf{u}^{\mathrm{T}})$ is the vorticity tensor, which are the asymmetric and symmetric components of $\nabla\mathbf{u}$, respectively; and $\| \mathbf{A} \| = \sqrt{\mathrm{tr}(\mathbf{A}\mathbf{A}^{\mathrm{T}})}$ is the Euclidean norm of a given tensor $\mathbf{A}$ (in our case Ω and S). Q indicates the local competition between the rotation rate and the deformation (or strain) rate, thus $\mathrm{Q} > 0$ means that the local rotational effect dominates [91].

3. λ_2-criterion, where λ_2 is the intermediate eigenvalue of the symmetric tensor $\Omega^2 + \mathrm{S}^2$, which relates the pressure P with the following relation

$$\Omega^2 + \mathrm{S}^2 = -\frac{\nabla\left(\nabla P\right)}{\rho} \tag{8.2}$$

This criterion defines a region as a vortex if every point in this region has $\lambda_2 < 0$, since $\lambda_2 < 0$ implies that the plane perpendicular to the local vortex axis has the local pressure minimum [40, 91].

4. N_k-criterion or kinematic vorticity number, which measure *"the quality of the rotation"*, instead of the local rotation rate given by $\| \Omega \|$. N_k is defined as

$$N_k = \frac{\| \Omega \|}{\| \mathrm{S} \|} \tag{8.3}$$

Thus, N_k is a pointwise measure of $| \omega |$ non-dimensionalized by the norm of the rate-of-strain tensor S, which gives the quality of the rotation regardless of the vorticity magnitude. For example, $N_k = \infty$ and $N_k = 0$ correspond to solid-body rotation and irrotational motion respectively, regardless of the $| \omega |$ value [91].

In figures 8.4, 8.5, 8.6, and 8.7 the vortical structures obtained using these four criteria are presented. For this case, a rectangular wing with aspect ratio equal to AR = 1 and elliptical cross-section (with a corresponding major axis $a = 0.5$ and minor axis $b = 0.0625$) is used. The wing is undergoing pure heaving motion as per equation eq. 2.21, at a Strouhal number equal to $St = 0.5$ and heaving amplitude equal to $h_a = 0.25$. The Reynolds number based on the wing chord is $Re = 500$. The results are shown for a non-dimensional time $t = 7.0$. The thresholds of each criteria were selected carefully so that the isosurfaces show approximately the same topological vortical structures.

It can be seen from figure 8.4, that the $| \omega |$-criterion, although capable of capturing the general vortical structures, has the disadvantage of also showing the shear layers near the wing surface and between the vortices. The Q, λ_2 and N_k criteria, show the vortical structure details more clearly and provide nearly identical structures; this is due to their mathematical and physical similarities [40, 63, 91, 178].

Additionally, we also use the pressure as a criteria for vortex identification. Local pressure minima are related to the presence of vortex structures, however, there is an inherent scale difference

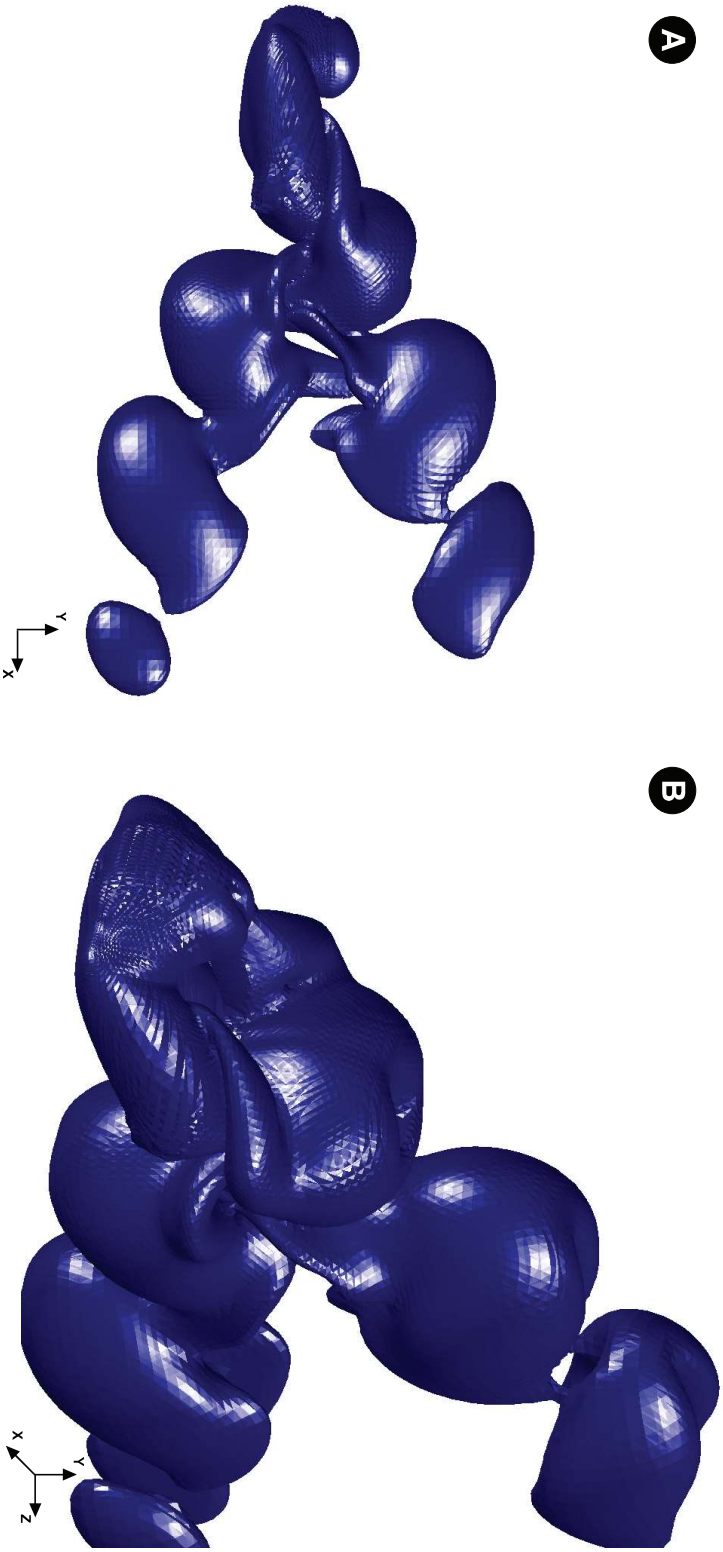

Figure 8.4: *Isosurfaces of* $|\omega|$*-criterion at the beginning of the upstroke (t=7.0). Flapping parameters:* $St = 0.5, h_a = 0.25, Re = 500$.

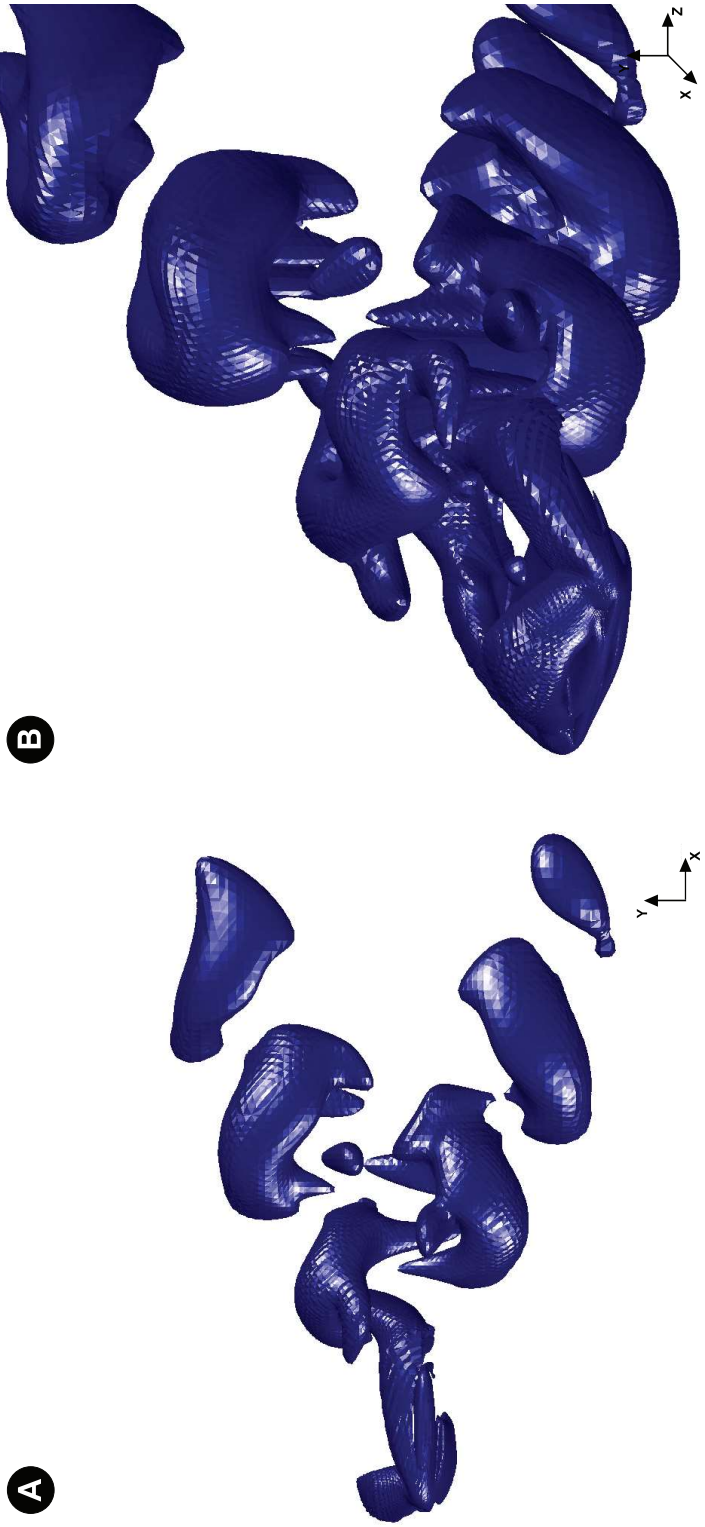

Figure 8.5: *Isosurfaces of Q-criterion at the beginning of the upstroke (t=7.0). Flapping parameters:* $St = 0.5, h_a = 0.25, Re = 500$.

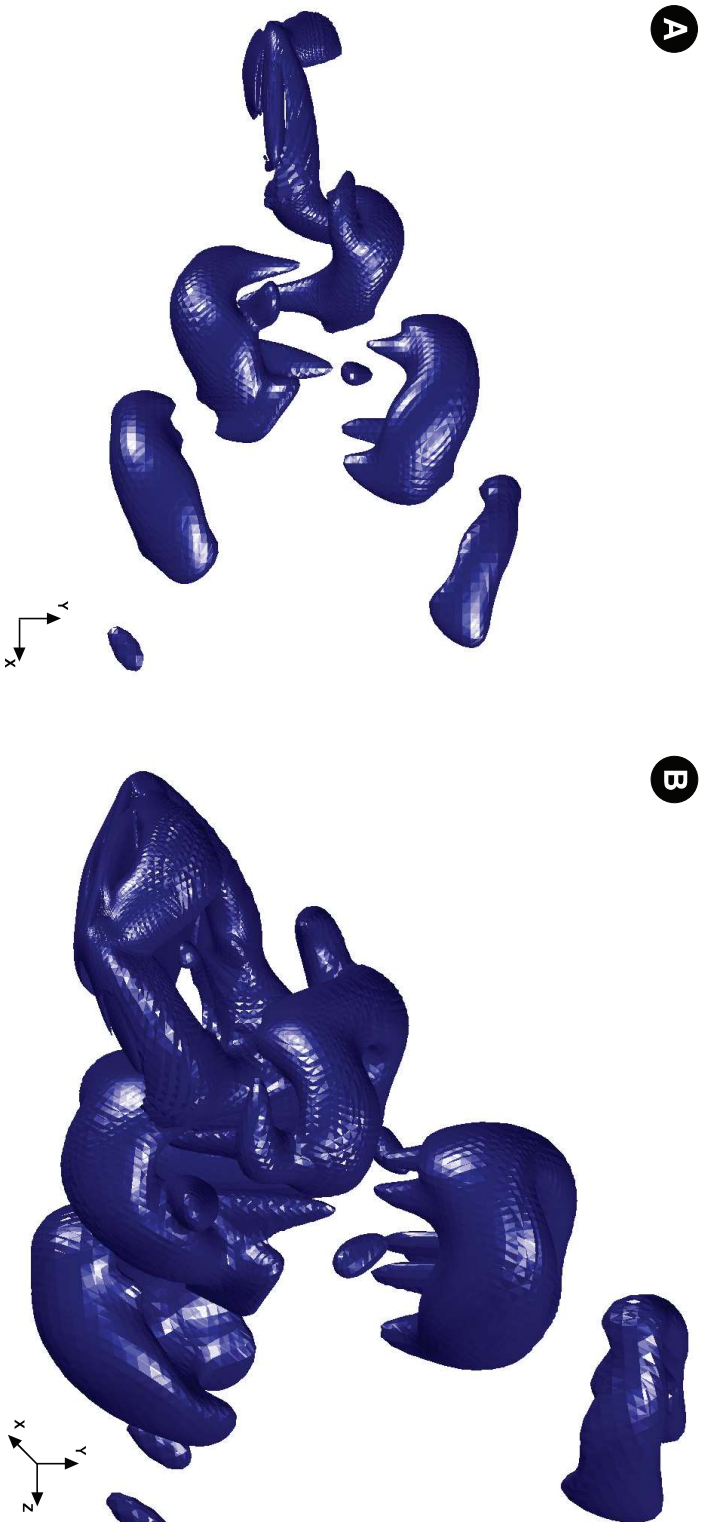

Figure 8.6: *Isosurfaces of λ_2-criterion at the beginning of the upstroke (t=7.0). Flapping parameters: $St = 0.5, h_a = 0.25, Re = 500$.*

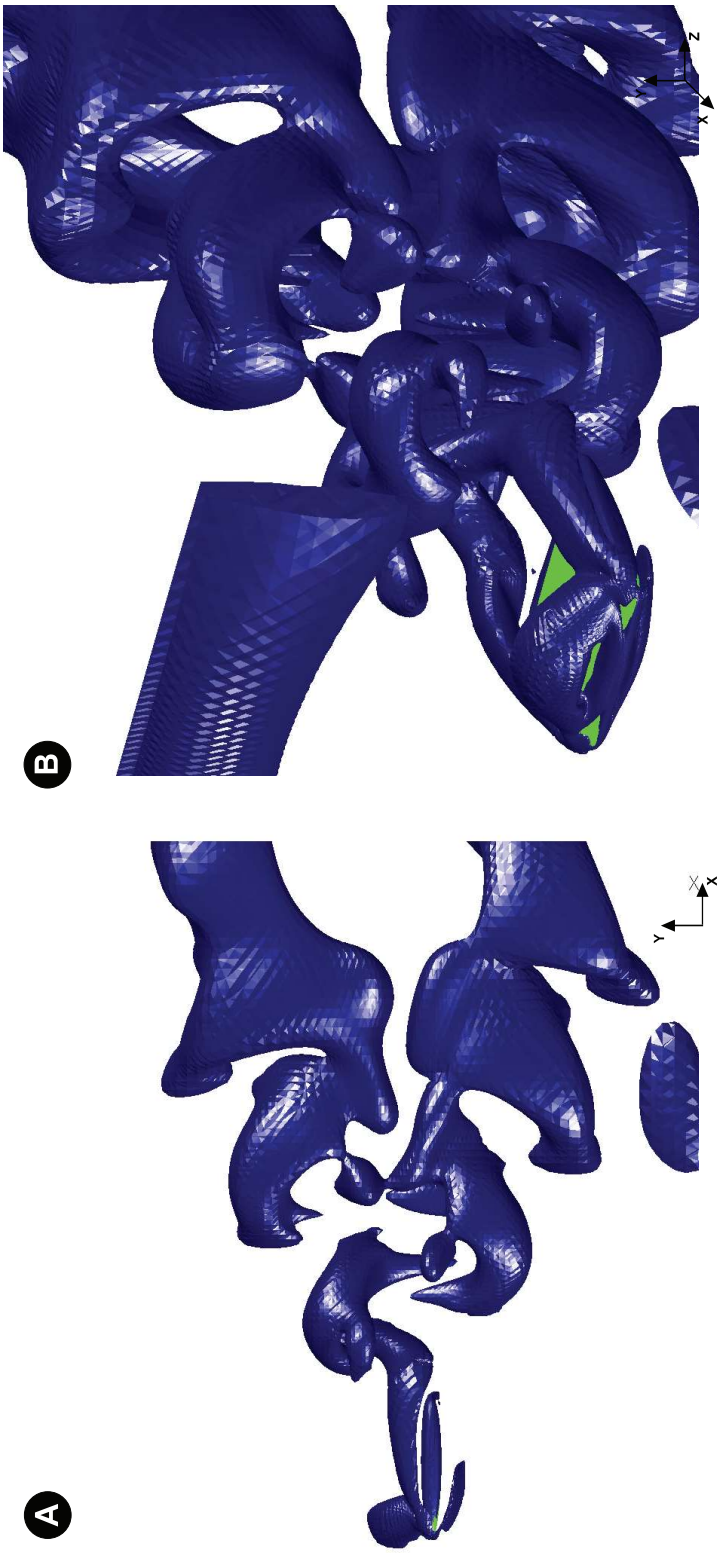

Figure 8.7: *Isosurfaces of N_k-criterion at the beginning of the upstroke (t=7.0). Flapping parameters: $St = 0.5, h_a = 0.25, Re = 500$.*

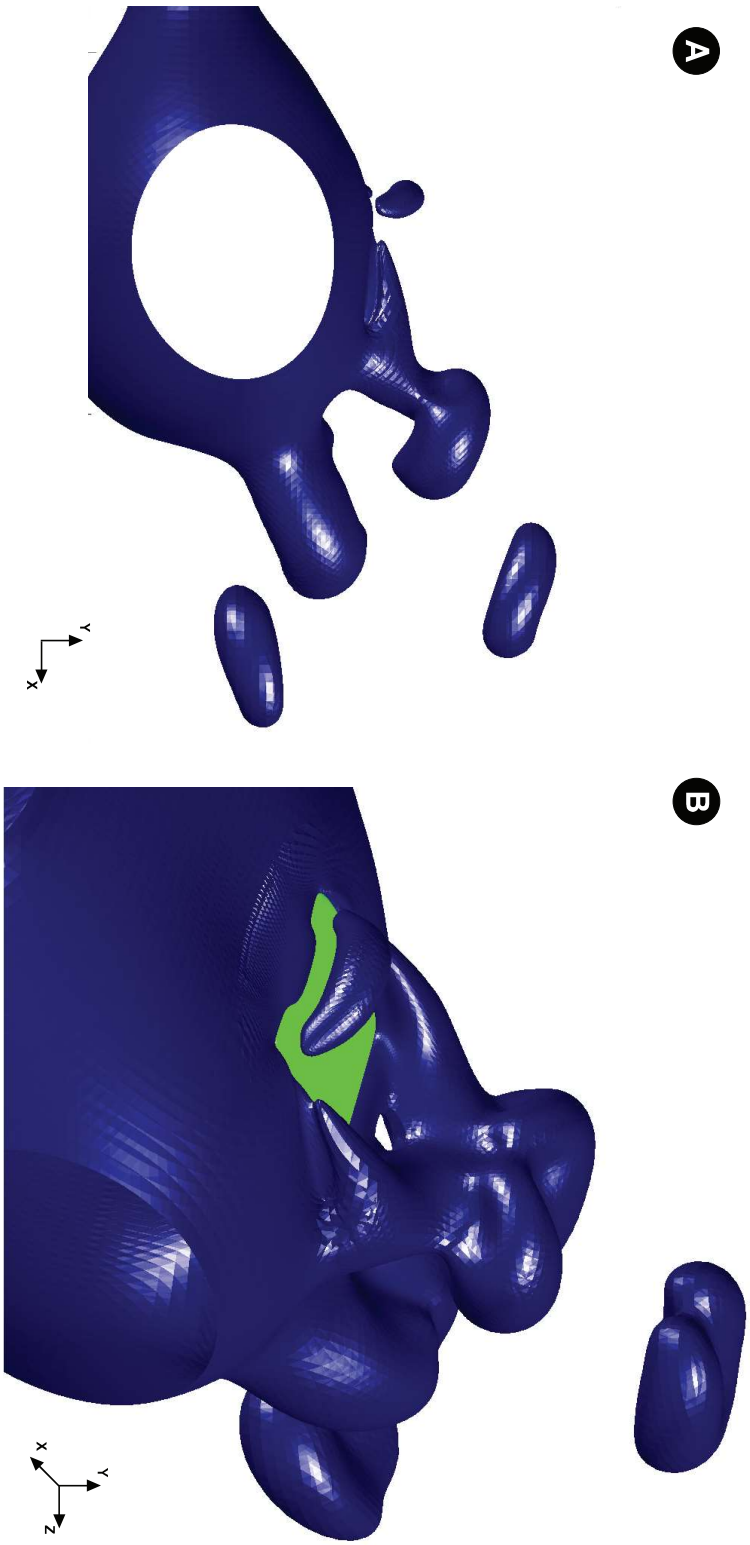

Figure 8.8: *Isosurfaces of pressure field at the beginning of the upstroke (t=7.0). Flapping parameters:* $St = 0.5, h_a = 0.25, Re = 500$.

between a vortex core and the associate low-pressure region and this makes the definition of vortices using isosurface of pressure a difficult task [91]. In figure 8.8, the isopressure surfaces are illustrated; in this figure, in order to capture the same vortical structures as in the velocity gradient tensor criteria, we choose low pressure values for the isosurfaces to be plotted. As it can be seen, in the far wake of the wing it is possible to capture vortex rings, while in the region close to the wing and in the upstream direction, the isopressure values extends farther away, making it difficult to identify the vortical structures.

Comparing all the previous criteria and since the Q-criterion offers more information about the local flow field, *i.e.*, $\mathrm{Q} < 0$ means the local deformation (strain) rate dominates over the rotation rate, we choose this as the main criterion for the wake topology characterization. Also, from a computational point of view it is found that the Q-criterion is less computational expensive than the λ_2 and N_k criteria.

8.4 Heaving Wing

In this section, we carry out a parametric study to asses the effect of Strouhal number St and reduced frequency k on the aerodynamic performance of a rigid finite-span heaving wing. A rectangular wing with aspect ratio equal to $\mathrm{AR} = 1$ and elliptical cross-section (with a corresponding major axis $a = 0.5$ and minor axis $b = 0.0625$) is used. The wing aspect ratio is defined as follows

$$\mathrm{AR} = \frac{S^2}{A} \tag{8.4}$$

where S is the wing span (wingtip-to-wingtip distance) and A is the wing area. For a rectangular wing, eq. 8.4 is simplified to

$$\mathrm{AR} = \frac{S}{c} \tag{8.5}$$

where c is the wing chord. High aspect ratios indicates long narrow wings, whereas a low aspect ratio indicates short, stubby wings.

The wing is undergoing pure heaving motion, wherein the wing cross-section center heaves in the vertical direction as per equation eq. 2.21. In table 8.1, we present the kinematics parameters governing this numerical experiment, where h_a is the heaving amplitude, f_h is the heaving frequency, St is the Strouhal number and k the reduced frequency. The numerical experiment is conducted at a Reynolds number equal to $Re = 500$.

The summary of results is presented in tabular form in table 8.2, where $\overline{c_t}$ is the average thrust coefficient and $\hat{c}_l$ is the maximum lift coefficient. Inspecting table 8.2, we can observe that as we increase St and k, the average thrust coefficient $\overline{c_t}$ and maximum lift coefficient $\hat{c}_l$ also increase (similar behavior as for the two-dimensional case). From the results obtained, for values of Strouhal number less than $St < 0.25$ we are in the drag production regime, for values of St between $0.25 < St < 0.35$ we produce little or no drag (or thrust), whereas for values of St higher than $St > 0.35$ we are in the thrust production regime. As in the two-dimensional cases, we observe two different behaviors of the aerodynamic forces for high and low reduced frequencies

Case number	Re	h_a	f_h	St	k
3DH1-1	500	0.15	0.5	0.15	1.57079
3DH1-2	500	0.075	1.0	0.15	3.14159
3DH1-3	500	0.25	0.5	0.25	1.57079
3DH1-4	500	0.125	1.0	0.25	3.14159
3DH1-5	500	0.35	0.5	0.35	1.57079
3DH1-6	500	0.175	1.0	0.35	3.14159
3DH1-7	500	0.5	0.5	0.5	1.57079
3DH1-8	500	0.25	1.0	0.5	3.14159

Table 8.1: *Kinematics parameters for the pure heaving wing case.*

k. Hence, it seems that for flapping wings, the flapping frequency also plays an important role in the vortex generation and shedding and, henceforth, on the aerodynamic forces.

Case number	St	k	$\overline{c_t}$	$\hat{c_l}$
3DH1-1	0.15	1.57079	-0.1832	1.5863
3DH1-2	0.15	3.14159	-0.1369	3.0548
3DH1-3	0.25	1.57079	-0.1407	2.9257
3DH1-4	0.25	3.14159	-0.0951	5.1792
3DH1-5	0.35	1.57079	-0.0766	4.5644
3DH1-6	0.35	3.14159	-0.0101	8.0671
3DH1-7	0.5	1.57079	0.0775	7.8142
3DH1-8	0.5	3.14159	0.1297	13.2126

Table 8.2: *Simulation results for the pure heaving wing case (positive $\overline{c_t}$ values indicate thrust production whereas negative $\overline{c_t}$ values indicate drag production).*

In table 8.3, we compare the results obtained for an infinite-span wing AR $= \infty$ (simulated as a two-dimensional case) against a finite-span wing. As it can be seen, the two-dimensional simulations highly overestimate the thrust and lift coefficients; obviously, this is due to the fact that three-dimensional effects (such as induced drag) are neglected. In figure 8.9, we show the spanwise vorticity contours for the case 3DH1-8 on the spanwise symmetry plane. For the infinite-span case (figure 8.9.A), we can clearly identify a reverse von Karman street which is indicative of thrust production, whereas for the finite-span wing (figure 8.9.C) the wake is a little bit different but we still can observe some common features with the infinite-span wing, such as the presence of the clockwise vortex V3 in the wake, the counter-clockwise vortex V2 shedding from the trailing edge and the clockwise LEV V1 on the top surface of the wing. However, in spite of these similarities, we also observe significant differences between the two wakes, the most important being the way how the wake is diffused in the streamwise direction for the finite-span case. In figure 8.9.D, we show the spanwise vorticity contours in the plane located at a distance equal to $d = 0.4 \times c$ measured from the wing symmetry plane; in this figure we can observe how the intensity of the vortices decrease as we move in the spanwise direction.

Let us now take a detailed look at the three-dimensional wake topologies shown in figures 8.10

Case number	St	k	$\overline{c_t}$ (3$\mathbb{D}$ case)	$\hat{c}_l$ (3$\mathbb{D}$ case)	$\overline{c_t}$ (2$\mathbb{D}$ case)	$\hat{c}_l$ (2$\mathbb{D}$ case)
3DH1-1	0.15	1.57079	-0.1832	1.5863	-0.1555	2.3144
3DH1-2	0.15	3.14159	-0.1369	3.0548	-0.1767	4.7388
3DH1-3	0.25	1.57079	-0.1407	2.9257	-0.1109	4.4637
3DH1-4	0.25	3.14159	-0.0951	5.1792	-0.04667	8.3741
3DH1-5	0.35	1.57079	-0.0766	4.5644	0.1177	7.2945
3DH1-6	0.35	3.14159	0.0101	8.0671	0.1682	13.2557
3DH1-7	0.5	1.57079	0.0775	7.8142	0.2857	13.6409
3DH1-8	0.5	3.14159	0.1297	13.2126	0.4823	25.3062

Table 8.3: *Simulation results for the pure heaving wing case. Comparison of the* 3$\mathbb{D}$ *results versus the* 2$\mathbb{D}$ *results (positive* $\overline{c_t}$ *values indicate thrust production whereas negative* $\overline{c_t}$ *values indicate drag production).*

and 8.11. From the three-dimensional perspective view of the wake topology (figure 8.10.B), it is clear that the wake of this finite-span wing has little resemblance with the two-dimensional case. This plot, as well as the side view, shows that the downstream wake of this wing consist of two sets of complex shaped vortex rings which convect at oblique angles about the centerline of the motion. In the figure we identify two rings R1 and R3 in the upper part of the wake and one ring R2 in the lower part of the wake. The process by which the vortex rings are formed can be explained by examining the vortex formation and shedding close to the wing. Let us consider the vortex V1 and V2, and their two associated wing-tip vortices TVL1 and TVR1 which constitute the four sides of a vortex loop, as shown in figures 8.10 and 8.11. Vortices V1 and V2 are connected by the wing-tip vortices TVL1 and TVR1 forming a vortex loop; as this vortex loop is convected it fully disconnect from the wing, forming in this way a vortex ring. It is also interesting to note that the vortex rings are themselves inclined with respect to the free-stream. It is also of interest that each vortex loop has two sets of thin contrails (C1 in figure 8.10.A), these structures are segments of the wing-tip vortices and as the vortex loops are convected downstream; these contrails become weaker and ultimately disappear as for vortex ring R1.

The wake topology plotted in figures 8.10 and 8.11 corresponds to a thrust production case (refer to case 3DH1-8 in table 8.2), in figures 8.12 and 8.13 we present the wake topology for a drag production case (refer to case 3DH1-2 in table 8.2). It is clear from these figures that the wake topology is very different from the one of the thrust generation case. In this case, as the vortex loops are convected downstream, they do not convert into vortex rings, instead, they keep their original shape and are diffused. In figures 8.12 and 8.13, it can be also observed that the wake height is very compact, opposite to that of the thrust production case. It can be also observed that the vortex loops are inclined in the direction opposite of their travel.

8.5 Flapping Wing

In this section, we present the results of a wing undergoing flapping motion (coupled heaving-and-pitching motion), where the wing cross-section heaves in the vertical direction as per eq. 2.21 and pitches about the spanwise axis at the wing cross-section center according to eq. 2.22. In table 8.4, we present the kinematic parameters governing this numerical experiment, where h_a is the heaving amplitude, α_a is the pitching amplitude, f is the flapping frequency (for both pitching

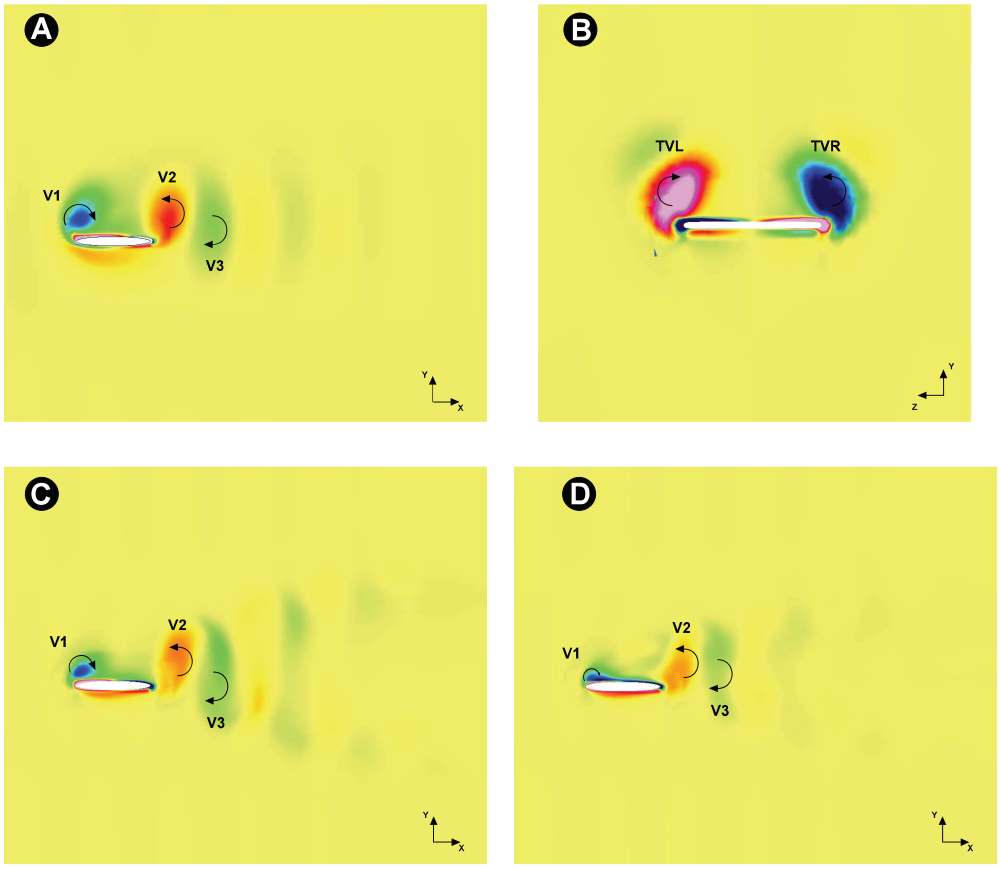

Figure 8.9: *Spanwise vorticity contours at the beginning of the upstroke (t=7.0). Flapping parameters:* $St = 0.5, h_a = 0.25, Re = 500$. *A) Spanwise vorticity contours for the infinite-span wing (2𝔻 case). B) Rear view of the wing-tip vortices for the finite-span wing, where TVL is the left wing-tip vortex and TVR is the right wing tip vortex. C) Spanwise vorticity contours for the finite-span wing at the symmetry plane (3𝔻 case). D) Spanwise vorticity contours for the finite-span wing in the plane located at a distance equal to* $d = 0.4 \times c$ *measured from the wing symmetry plane (3𝔻 case).*

and heaving motion), St is the Strouhal number and k the reduced frequency. The numerical experiment was conducted at a Reynolds number equal to $Re = 500$ and the finite-span wing used is exactly the same as that used in the previous section.

Case number	Re	h_a	$\alpha_a(^\circ)$	f	St	k
3DF1	500	0.25	5	1.0	0.5	3.14159
3DF2	500	0.25	10	1.0	0.5	3.14159
3DF3	500	0.25	20	1.0	0.5	3.14159

Table 8.4: *Kinematic parameters for the flapping wing case.*

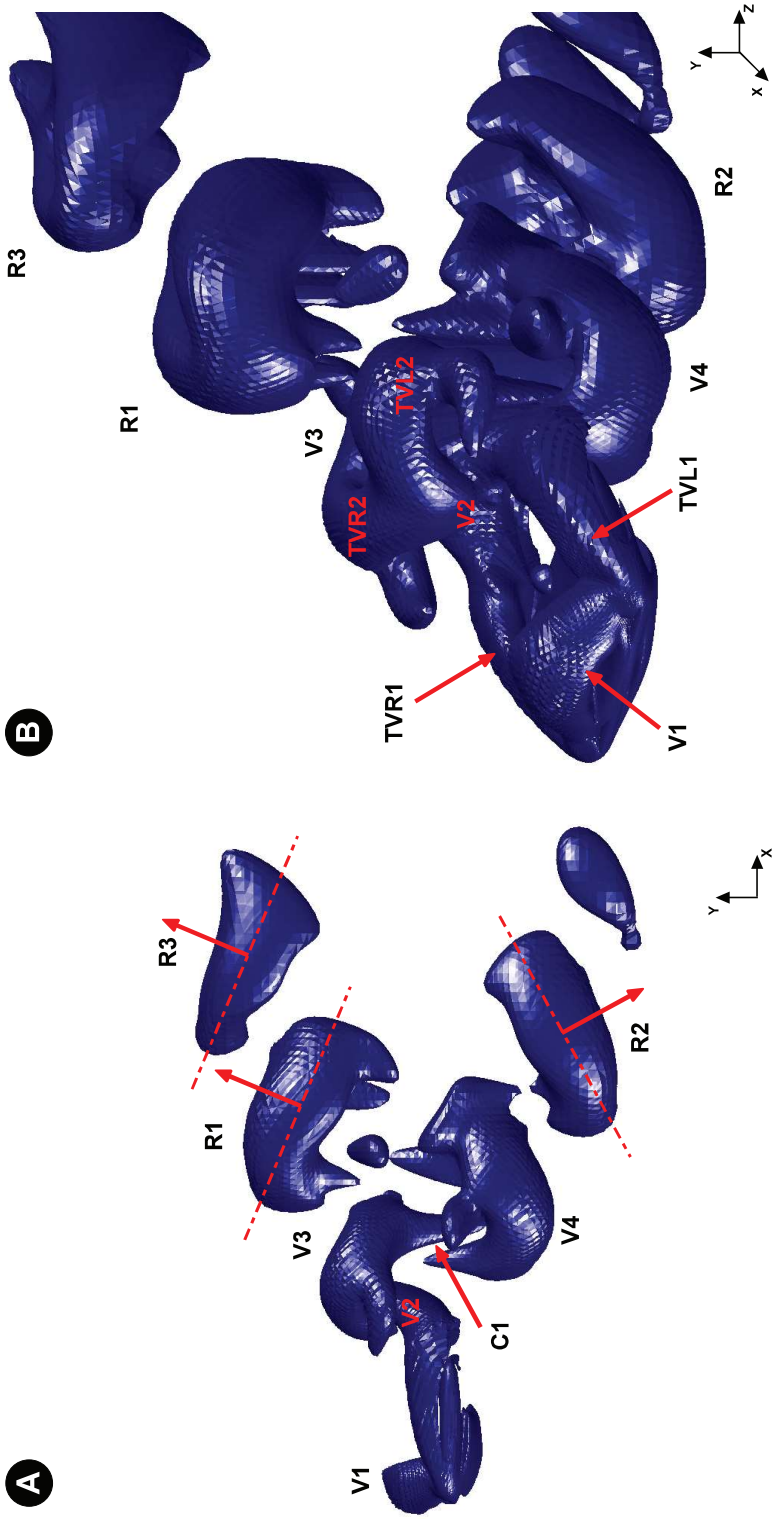

Figure 8.10: *Vortex topology at the beginning of the upstroke (t=7.0). Flapping parameters:* $St = 0.5, h_a = 0.25, Re = 500$. *A) Side view. B) Perspective view.*

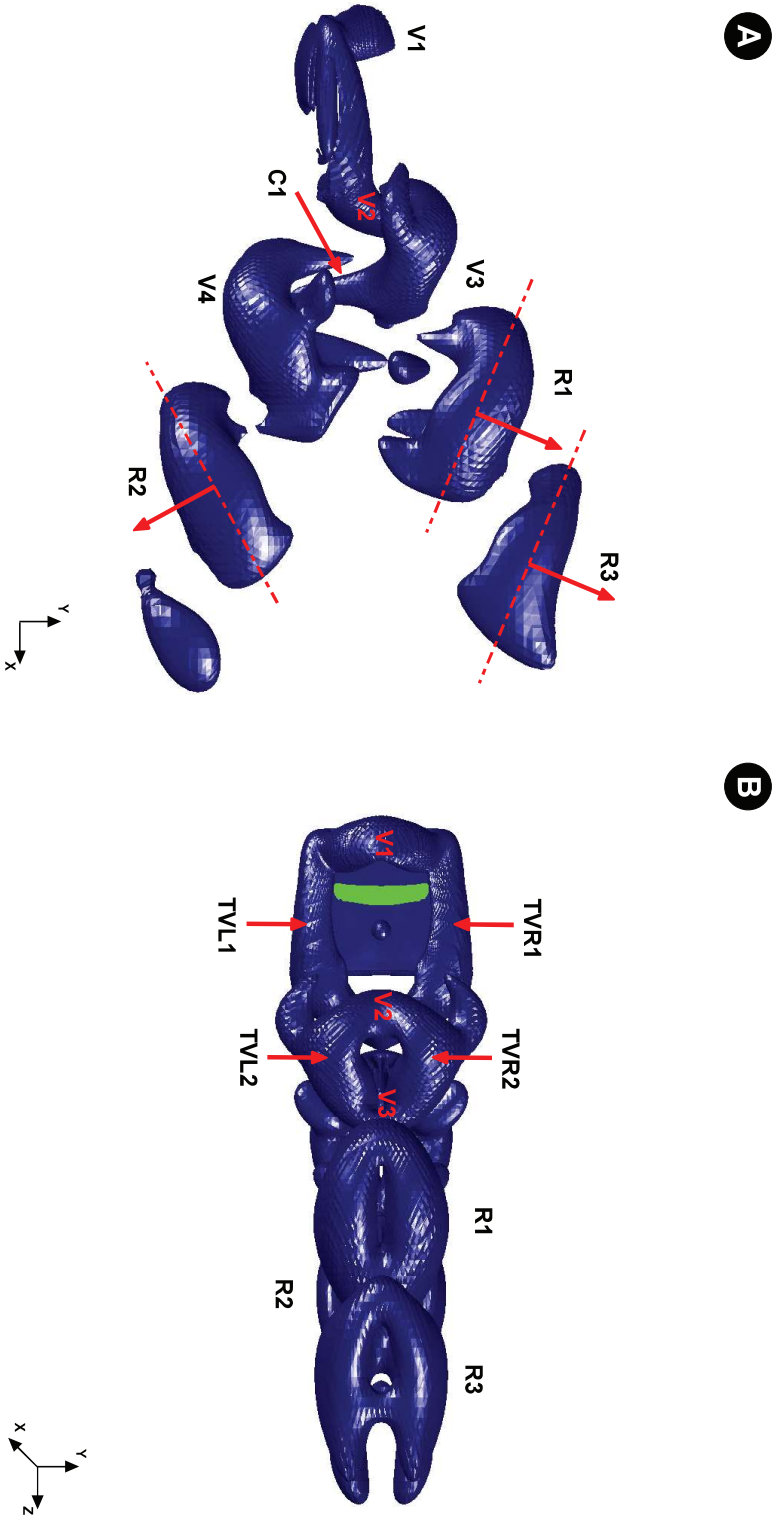

Figure 8.11: *Vortex topology at the beginning of the upstroke (t=7.0). Flapping parameters: $St = 0.5, h_a = 0.25, Re = 500$. A) Side view. B) Top view.*

Figure 8.12: *Vortex topology at the beginning of the upstroke (t=7.0). Flapping parameters:* $St = 0.15, h_a = 0.075, Re = 500$. *A) Side view. B) Perspective view.*

Figure 8.13: *Vortex topology at the beginning of the upstroke (t=7.0). Flapping parameters:* $St = 0.15, h_a = 0.075, Re = 500$. *A) Side view. B) Top view.*

In table 8.5, we present the computed average thrust coefficient $\overline{c_t}$ and maximum lift coefficient $\hat{c}_l$ for the cases shown in table 8.4, additionally, for purposes of comparison we also show the results for the case 3DH1-8 (see table 8.4), which corresponds to pure heaving motion.

Case number	St	h_a	$\alpha_a(^\circ)$	f	$\overline{c_t}$	$\hat{c}_l$
3DH1-8	0.5	0.25	0	1.0	0.1297	13.2126
3DF1	0.5	0.25	5	1.0	0.1307	14.7020
3DF2	0.5	0.25	10	1.0	0.1402	10.2724
3DF3	0.5	0.25	20	1.0	0.1591	6.8924

Table 8.5: *Simulation results for the flapping wing case.*

The typical wake topologies for the cases 3DF2 and 3DF3 are shown in figures 8.14 and 8.15, respectively. The figures show the three-dimensional perspective view, side view and top view. As for the heaving case, the key feature observed here is the presence of two interconnected vortex loops that slowly convert into vortex rings as they are convected downstream. Additionally, in figures 8.16 and 8.17 we plot the streamlines for a given instant during the downstroke, notice in these figures the wake evolution and the wing-tip vortices.

8.6 Aspect Ratio Influence on the Aerodynamics Performance

In this section, we consider the effect of aspect-ratio AR on the aerodynamic performance. In this case, the wing is undergoing pure heaving motion as per equation 2.21. The kinematics and geometry parameters are shown in table 8.6, where h_a is the heaving amplitude, AR is the aspect ratio, f_h is the heaving frequency, St is the Strouhal number and k the reduced frequency.

Case number	Re	h_a	f_h	AR	St	k
3DAR1	500	0.175	1.0	1.0	0.35	3.14159
3DAR2	500	0.175	1.0	2.0	0.35	3.14159
3DAR3	500	0.175	1.0	3.0	0.35	3.14159
3DAR4	500	0.175	1.0	4.0	0.35	3.14159

Table 8.6: *Kinematics and geometrical parameters for the heaving wing case with different aspect ratios.*

The main purpose of this numerical experiment, is to assess the effect of AR on the aerodynamic forces of finite-span wings and to study if the assumption of two-dimensionality have some validity for three-dimensional cases. Hereafter, the results are presented in tabular form in table 8.7, where $\overline{c_t}$ is the average thrust coefficient and $\hat{c}_l$ is the maximum lift coefficient. Inspecting table 8.7, we can observe that as we increase the wing AR, the computed values of the aerodynamics forces also increase and this is chiefly to the fact of the high area of high AR wings and to the decrease of three-dimensional effects in long wings. This observation lead us to think that the assumption of two-dimensionality has some validity for birds and insects, where the wings of many species tend to have relatively large aspect ratio.

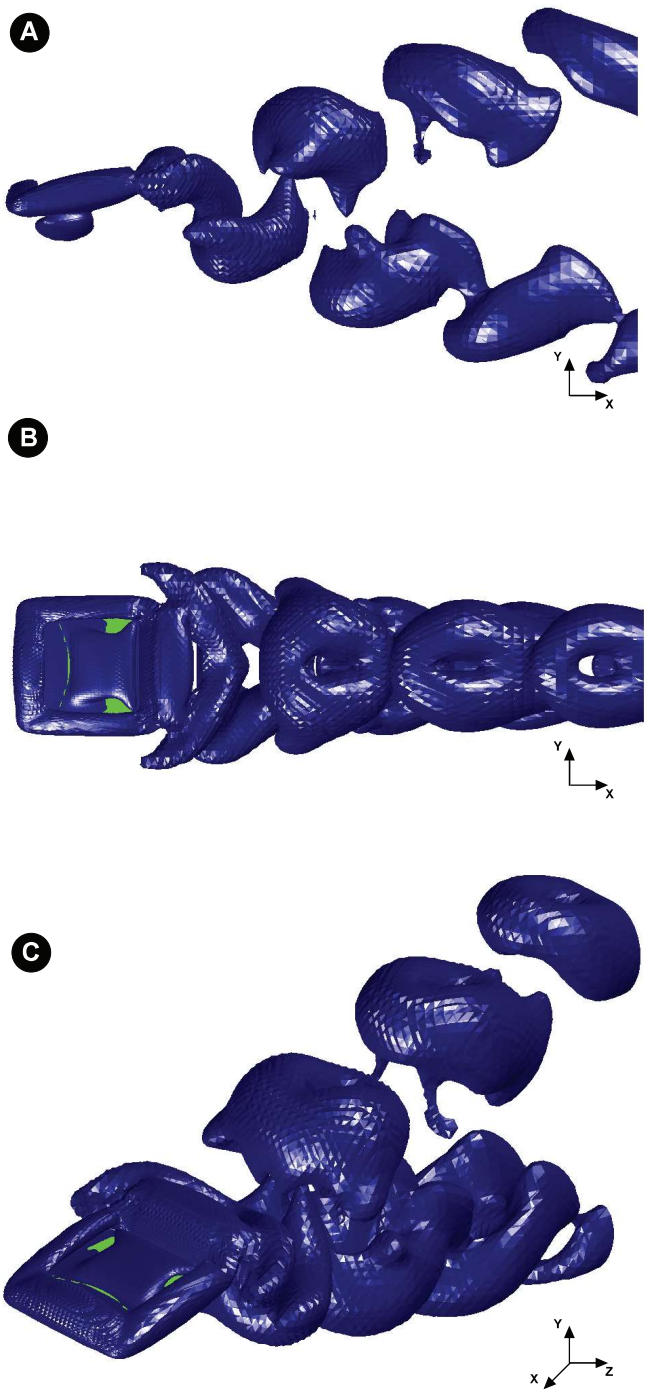

Figure 8.14: *Vortex topology during downstroke (t=6.75). Flapping parameters:* $St = 0.5, h_a = 0.25, \alpha_a = 10°, Re = 500$. *A) Side view. B) Top view. C) Perspective view.*

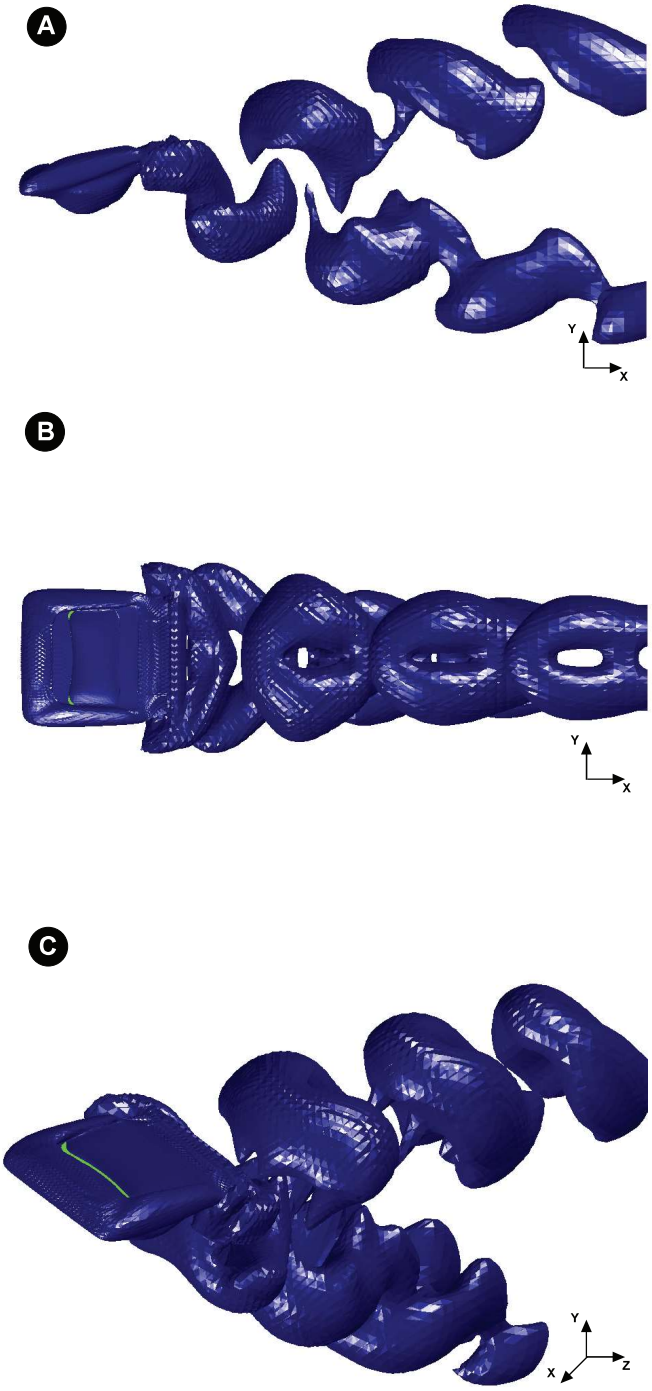

Figure 8.15: *Vortex topology during downstroke (t=6.75). Flapping parameters:* $St = 0.5, h_a = 0.25, \alpha_a = 20°, Re = 500$. *A) Side view. B) Top View. C) Perspective view.*

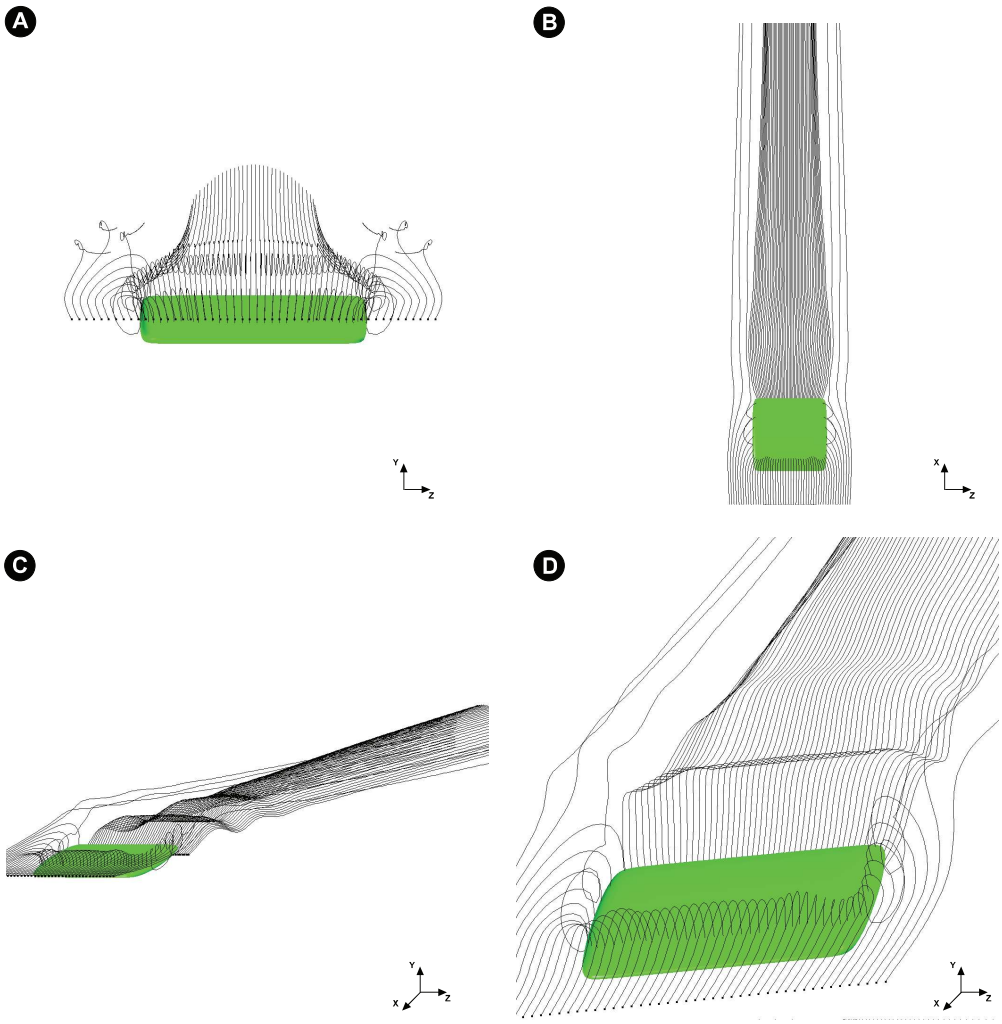

Figure 8.16: *Streamlines visualization during downstroke (t=6.75). Flapping parameters:* $St = 0.5, h_a = 0.25, \alpha_a = 10°, Re = 500$. *A) Front view. B) Top View. C) Perspective view. D) Perspective view.*

Case number	AR	$\overline{c_t}$	$\hat{c_l}$
3DAR1	1	-0.0101	8.0671
3DAR2	2	0.0356	16.5643
3DAR3	3	0.0784	33.8802
3DAR4	4	0.0864	49.5601
3DH1-6	∞	0.1682	13.2557

Table 8.7: *Simulation results for the heaving wing case with different aspect ratios (positive* $\overline{c_t}$ *values indicate thrust production whereas negative* $\overline{c_t}$ *values indicate drag production).*

8.7 Rolling Wing

In this section, we simulate a rectangular wing rolling about its traveling axis (root-flapping motion). The wing aspect ratio for this case is equal to AR = 2 and its cross-section is elliptical

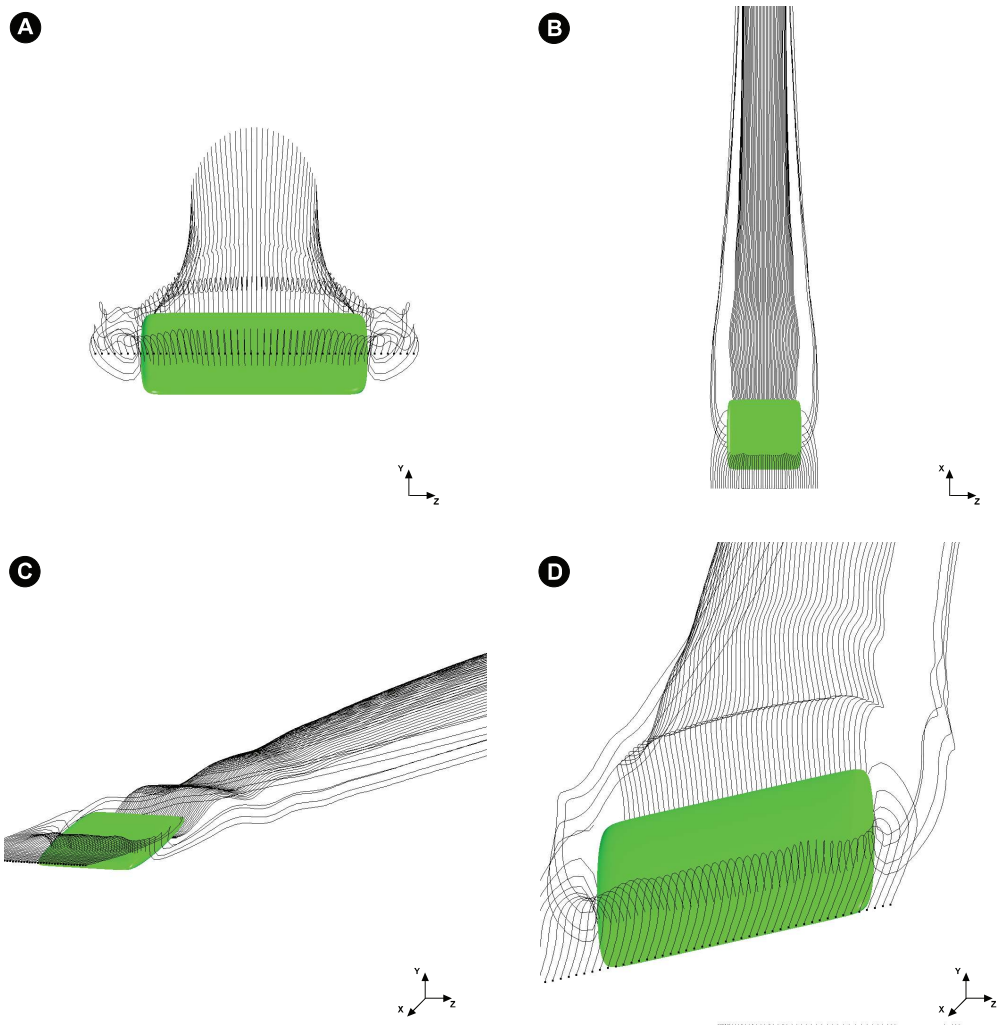

Figure 8.17: *Streamlines visualization during downstroke (t=6.75). Flapping parameters:* $St = 0.5, h_a = 0.25, \alpha_a = 20°, Re = 500$. *A) Front view. B) Top View. C) Perspective view. D) Perspective view.*

(with corresponding major and minor axis equal to $a = 0.25$ and $b = 0.025$). In this case, the wing is hinged at one wing-tip and is rolling about the traveling axis as per eq. 2.22 (where the traveling axis and the hinged point are collinear). The Strouhal number for this case is based in the dorsoventral stroke angle as proposed by Taylor *et al.* [182] and is computed as follows

$$St = \frac{S\ sen\,(\phi/2)\, f_{roll}}{U} \tag{8.6}$$

where S is the wing span, ϕ is the dorsoventral stroke angle or positional angle (see figure 2.21), f_{roll} is the wing rolling frequency and U the forward velocity. The kinematic parameters for this case are shown in table 8.8. The numerical experiment is conducted at a Reynolds number equal to $Re = 500$.

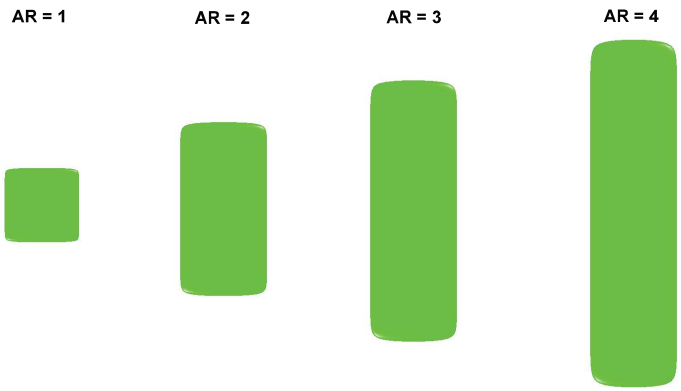

Figure 8.18: *Different wing platforms used for the study of aspect ratio influence on the aerodynamic performance.*

Case number	Re	$\phi(^\circ)$	f_{roll}	St
3DRL1	500	12.5	1.0	0.10
3DRL2	500	30.0	1.0	0.25
3DRL3	500	45.0	1.0	0.38

Table 8.8: *Kinematics parameters for the rolling wing case.*

Usually, flapping wing studies only consider heaving or coupled heaving-and-pitching motions. Hereafter, we carry out this numerical study in order to check whether this mode of motion shows similar features to those of the heaving or coupled heaving-and-pitching motions, we also study the validity of the use of the Strouhal number for wake characterization.

In table 8.9 we show the simulation results for this case, as it can be seen, for values less than $St < 0.25$ we are in the drag production regime, for values approximately equal to $St = 0.25$ we produce little or no drag (or thrust), whereas for values higher that $St > 0.25$ we are in the thrust production regime. From these results, it is clear that this behavior is similar to that of heaving or coupled heaving-and-pitching motions. Comparing these results with the results for pure heaving or coupled heaving-and-flapping motions, we found that the latter motions generate larger vortices and forces than root-flapping motion, presumably because the average velocity is higher across the span, but otherwise the same wake regimes occurs at similar Strouhal numbers.

Case number	St	$\overline{c_t}$	$\hat{c_l}$
3DRL1	0.10	-0.1485	0.5991
3DRL2	0.25	-0.0843	2.3637
3DRL3	0.38	0.0748	4.8749

Table 8.9: *Summary of results for the rolling case with different dorsoventral stroke angles (positive $\overline{c_t}$ values indicate thrust production whereas negative $\overline{c_t}$ values indicate drag production).*

In figures 8.19, 8.20 and 8.21, the three-dimensional wake structures for the cases shown in table 8.8 are illustrated. The salient feature that needs to be pointed out from these figures is the absence of any link or the presence of a very weak link between the root-tip vortex and the leading and trailing edge vortices. We also observe that for the case of $St = 0.10$, there is no connection at all between both wing-tip vortices and the trailing and leading edge vortices; this is clearly due to the fact that the tip vortices generated at this low Strouhal number have very low strength. Additionally, in figures 8.22 and 8.23 we plot the streamlines for four different instants during the downstroke, notice in these figures the wake evolution and the wing-tip vortices at the moving tip.

8.8 Summary

In this chapter, we have presented several results for finite-span flapping wings. The simulations show that the wake of thrust producing, rigid finite-span flapping wings is formed by two sets of interconnected vortex ring loops that slowly convert into vortex rings as they are convected downstream. It was also observed that the vortex rings are themselves inclined with respect to the free-stream; the angle of inclination of the vortex rings is found to be in the direction of their travel and in the streamwise direction for thrust producing configurations; whereas for drag producing configurations the angle of inclination is opposite to the direction of travel of the streamwise flow. It was also noted the presence of thin contrails that link the vortex loops, these structures are segments of the wing-tip vortices and as the vortex loops are convected downstream, these contrails become weaker and ultimately disappear. In general, the observed structures are qualitatively similar to those observed in the experiments by Parker *et al.* [138].

In this chapter, the effect of aspect ratio AR on the aerodynamic forces of finite-span wings was also assessed. It was observed that as we increase the wing AR, the aerodynamic forces also increase and this is chiefly attributed to the large area of high aspect ratio wings and to the decrease of three-dimensional effects in long wings. This observation lead us to think that the assumption of two-dimensionality has some validity for birds and insects, where the wings of many species tend to have relatively large aspect ratio, *e.g.*, large seabirds such as Albatrosses have aspect ratios about 13 to 15, land birds such as Eagles and Vultures have aspect ratios of roughly 6 to 8 and insects such as the Bumblebee and the Crane fly have aspect ratios between 6 to 7 [3].

Finally, besides the heaving and coupled heaving-and-pitching motions, we have also studied the root-flapping motion characteristic of flying animals, which as far as the author is aware, still remains virtually unexplored. From the results obtained it is found that, indeed, root-flapping motion produces wake structures similar to those of heaving or coupled heaving-and-pitching motions, but with the difference that the latter motions generate larger vortices and forces than root-flapping motion, presumably because the average velocity is higher across the span; aside from this, similar wake regimes occurs at similar Strouhal numbers.

Figure 8.19: *Vortex topology for the rolling wing case (t=5.0). Flapping parameters:* $St = 0.10, f_{roll} = 1.0, Re = 500$. *A) Perspective view. B) Top view. In this view the right wing-tip corresponds to the hinged extreme. C) Side view.*

Figure 8.20: *Vortex topology for the rolling wing case (t=5.0). Flapping parameters:* $St = 0.25, f_{roll} = 1.0, Re = 500$. *A) Perspective view. B) Top view. In this view the right wing-tip corresponds to the hinged extreme. C) Side view.*

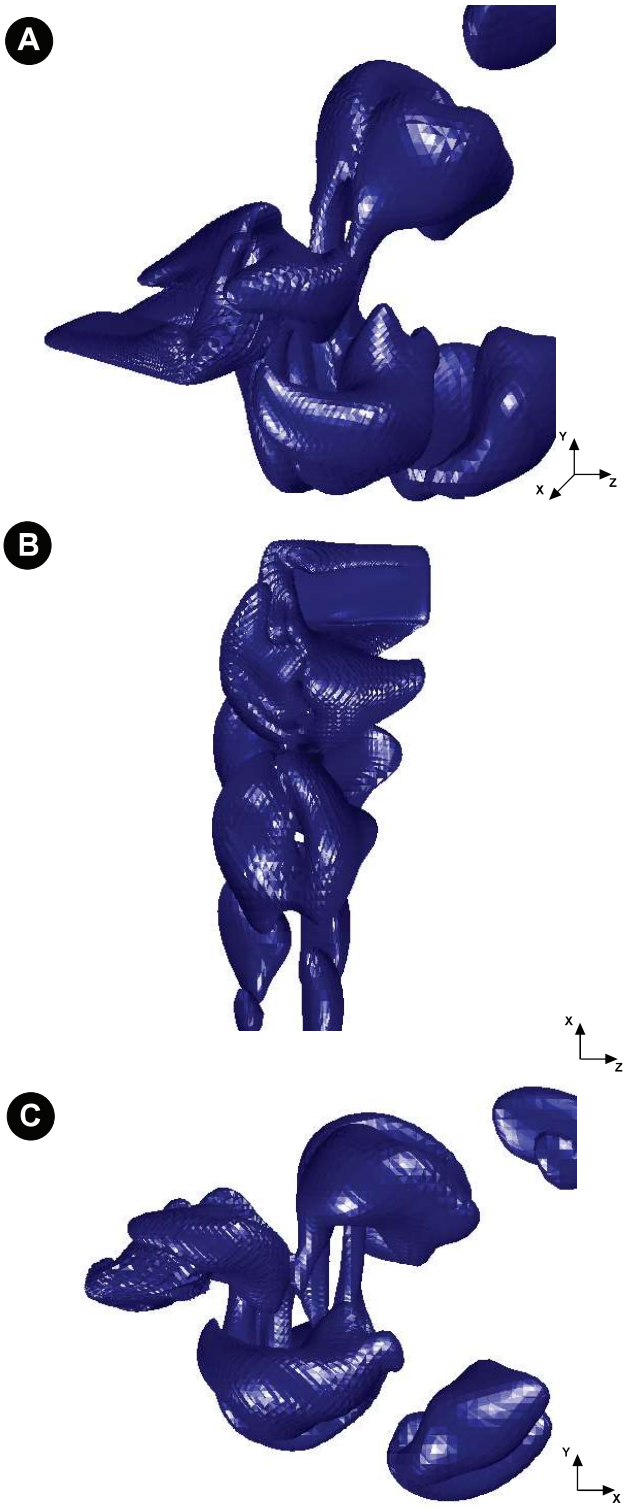

Figure 8.21: *Vortex topology for the rolling wing case (t=5.0). Flapping parameters:* $St = 0.38, f_{roll} = 1.0, Re = 500$. *A) Perspective view. B) Top view. In this view the right wing-tip corresponds to the hinged extreme. C) Side view.*

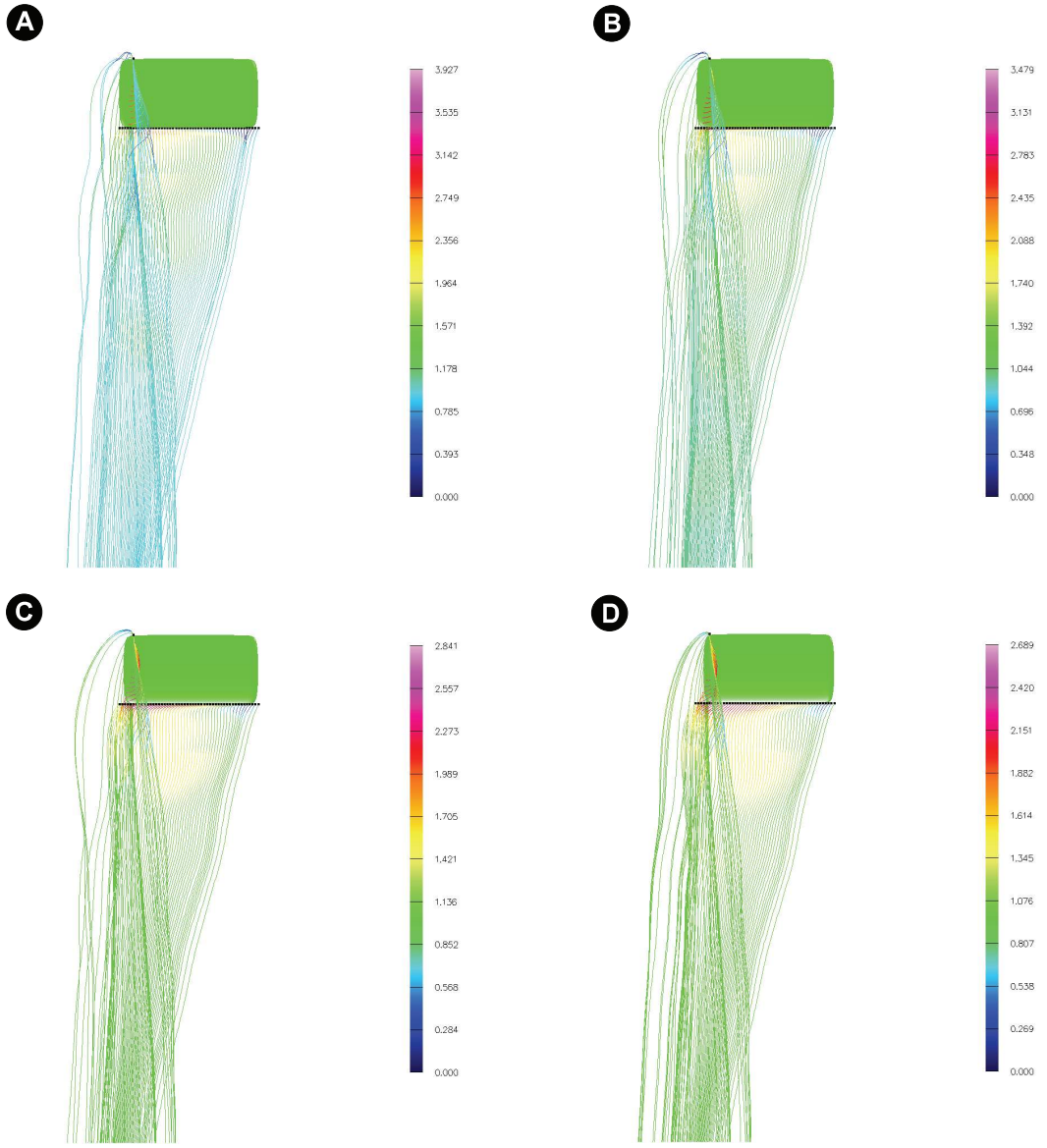

Figure 8.22: *Streamlines visualization during downstroke (top view), the streamlines are colored according to the velocity magnitude values. In this view the right wing-tip corresponds to the hinged extreme. Flapping parameters:* $St = 0.38, f_{roll} = 1.0, Re = 500$. *A) t=5.0 B) t=5.05 C) t=5.10 D) t=5.15.*

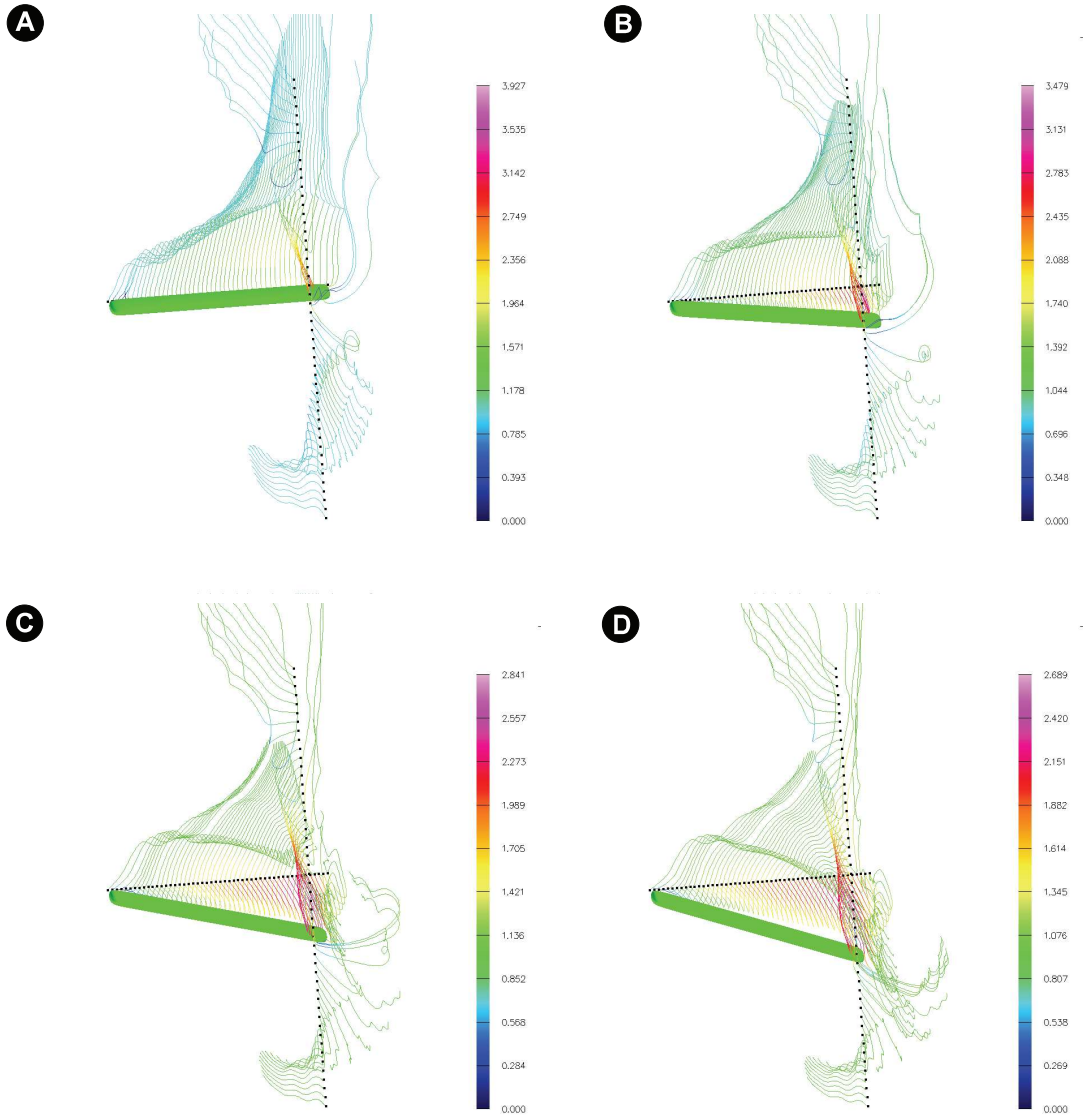

Figure 8.23: *Streamlines visualization during downstroke (perspective view), the streamlines are colored according to the velocity magnitude values. In this view the left wing-tip corresponds to the hinged extreme. Flapping parameters:* $St = 0.38, f_{roll} = 1.0, Re = 500$. *A) t=5.0 B) t=5.05 C) t=5.10 D) t=5.15.*